



# An analytical model for a liquid plug moving in curved microchannels

Zhizhao Che, Teck Neng Wong<sup>\*</sup>, Nam-Trung Nguyen

School of Mechanical and Aerospace Engineering, Nanyang Technological University, 50 Nanyang Avenue, Singapore 639798, Singapore

## ARTICLE INFO

### Article history:

Received 24 March 2009  
Received in revised form 12 December 2009  
Accepted 12 December 2009  
Available online 27 January 2010

### Keywords:

Curved microchannel  
Plug flow  
Analytical model  
Vortex  
Flow resistance

## ABSTRACT

Droplet-based microfluidics has wide applications and triggers numerous researchers' interest. It is significant to study the flow field inside a droplet moving in microchannels. This paper presents an analytical method to investigate the flow field inside a confined droplet (a plug) moving in curved microchannels with high aspect ratio. The flow field is compared against a one-dimensional solution and the published experimental data. The effects of the plug length and the curvature on the flow pattern and the flow resistance are studied. The results suggest that the vortex pattern of the plug can be controlled by designing the channel geometry.

© 2010 Elsevier Ltd. All rights reserved.

## 1. Introduction

Droplet-based microfluidics offers promising opportunities in life science, chemistry, and biomedical science. It can be used for drug delivery, point of care diagnostics, microreactors, organic synthesis, gene-expression analysis, drug screening, etc. Being different from continuous microfluidics, droplet-based microfluidics manipulates fluids in a discrete manner [1]. This feature offers the ability to actuate and manipulate droplets precisely and individually. Compared to continuous flow microfluidics, droplet-based microfluidics has the advantages of less sample requirement, minimized cross-contamination and scalability. Droplet-based microfluidic devices can even offer logic functions [2,3]. Droplets can be actuated and manipulated by pressure [4], thermocapillarity [5–7], electrowetting [8,9], magnetic forces [10], optically induced forces [11], surface acoustic wave [12,13] and others. For further information on droplet-based microfluidics, reader can refer to a review by Teh et al. [1].

Knowing the flow field inside droplets is important to understand the flow phenomena paving the way for related applications. Different methods are utilized to study the flow field inside droplets. For experiment, micro particle image velocimetry ( $\mu$ PIV) can offer the flow details in droplets [14–19]. Dye is also used to show the flow patterns inside droplets [20,21]. As for computational methods, according to whether predicting the droplet shape, two types of methods are widely used. The first type is to assume the interface shape, such as flat interfaces [22] or even assume the

interfaces as static walls with non-slip boundary conditions [19,23,24]. Most of the numerical simulations through this approach were carried out in two-dimensional (2D) mode. Computation time was saved without predicting the interface shape, and reasonable results were obtained. However, the static wall condition is not easily satisfied especially when the fluid of the adjacent plug has large shear effect at the interface. The other type of computational method needs to use the interface predicting technique such as front-tracking [25], volume-of-fluid [26,27], level-set [28], moving-grid [29] and etc. These approaches are usually complex and computation-time consuming. This is not favourable especially for applications in which additional processes need to analyze, such as chaos analysis in mixing process [30–32]. On the contrary, with an explicit fully analytical model, analysis is much more convenient as it can be performed directly on the known flow fields. For analytical methods for droplet flow, Handique and Burns [33] assumed that the flow in the droplet is fully developed one-dimensional (1D) flow. This parabolic velocity profile is valid only when the plug is long. Another analytical model available related to the droplet flow in microchannels, to our best knowledge, needs to assume that the channel width is much larger than the dimension of the droplet [34,35]. Therefore, this method is not practical for the case of a confined droplet, or a plug, which refers to droplets contacting the wall of the channel. This happens when the droplet is sufficiently large. When the wall of the microchannel is hydrophilic, plugs exist even if the droplet is relatively short [29].

In this paper, we present a 2D analytical model to investigate the flow pattern inside a liquid plug moving in a curved microchannel. This proposed method for curved channel is a more general case than that of the 1D model in a straight channel. In the

<sup>\*</sup> Corresponding author.

E-mail address: [mtnwong@ntu.edu.sg](mailto:mtnwong@ntu.edu.sg) (T.N. Wong).

## Nomenclature

$C$	constant coefficient (–)
$C_f$	plug resistance coefficient (–)
$f$	Moody friction factor (–)
$L$	length of the plug (m)
$M$	moment of force (N m)
$P$	pressure (Pa)
$r$	radial coordinate in polar coordinate system (m)
$R$	diameter of the curved microchannel (m)
$Re$	Reynolds number (–)
$u$	velocity (m/s)
$V$	peripheral speed (m/s)
$w$	width of the microchannel (m)
$x$	radial position of the vortex centre (–)

### Greek symbols

$\alpha$	eigenvalues (–)
$\theta$	angular coordinate in polar coordinate system (rad)
$\mu$	dynamic viscosity of fluid (Pa s)
$\sigma$	surface tension (N/m)
$\tau$	stress (Pa)
$\varphi$	stream function (m <sup>2</sup> /s)

$\omega$	angular velocity of the plug moving in the curved micro-channel (rad/s)
----------	---

### Subscripts

avg	average
adv	advancing end of the plug
A	inner vortex in the plug
B	outer vortex in the plug
rec	receding end of the plug
max	maximum of stream function
min	minimum of stream function
1	outer wall of the curved microchannel
2	inner wall of the curved microchannel

### Superscript

$\wedge$	dimensionless variables (–)
----------	-----------------------------

### Abbreviations

1D	one-dimensional
2D	two-dimensional
FFT	finite Fourier transform
$\mu$ PIV	micro particle image velocimetry

next section, we describe the flow governed by a biharmonic equation together with its boundary conditions. Next, the equation is solved in dimensionless form using Finite Fourier Transform (FFT) method [36]. The result is compared against a 1D solution and the published experimental data from  $\mu$ PIV [14]. Then we present the result of the analytical solution and analyze the effects of the plug length and the channel curvature on the flow pattern. Before we conclude, the resistance of the plug flow is analyzed.

## 2. Analytical model

### 2.1. Problem description and assumptions

Fig. 1 shows the model of a liquid plug moving in a curved microchannel. The shaded area is the liquid plug of interest. The surrounding area is an immiscible phase such as air. The two ends of the liquid plug are assumed to be flat. The radii of the outer and inner walls of the channel are  $R_1$  and  $R_2$ , respectively. Therefore, the width of the channel is  $w = R_1 - R_2$ . The plug length,  $L$ , is measured along the centre line of the channel. The plug is moving in the anticlockwise direction with an angular velocity  $\omega$ , around the centre point of the curved channel  $O$ .

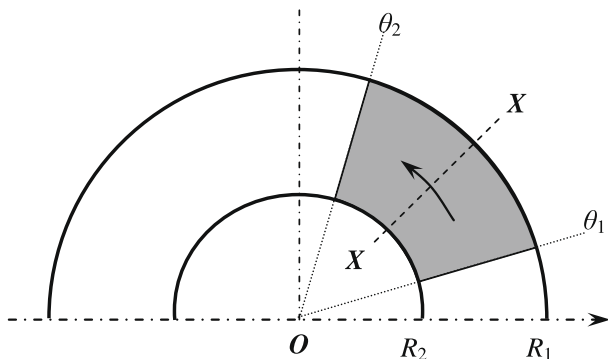


Fig. 1. Schematic of the flow in a curved microchannel.

A polar coordinate is built with the origin at the centre  $O$  of the curved channel, as shown in Fig. 1. The plug takes the region from  $\theta_1$  to  $\theta_2$ . The middle cross section of the plug is indicated by  $X-X'$  at  $\theta = (\theta_1 + \theta_2)/2$ . In order to simplify the equations, the coordinate system is rotating with an angular velocity  $\omega$ . In this way, the liquid plug is stationary relative to the rotating frame of reference, while the outer and inner walls of the channel are at peripheral speeds of  $V_{R1}$  and  $V_{R2}$ , and in the clockwise direction, where  $V_{R1} = \omega R_1$  and  $V_{R2} = \omega R_2$ . As the velocity of the liquid plug is small, the centripetal acceleration, due to the non-inertial frame of reference, can be neglected in the momentum equation.

In our analysis, the following assumptions are made:

- (1) Stokes flow with low Reynolds number exists inside the plug. The transient term and the convection term are neglected in the momentum equation.
- (2) No body force is considered. The gravity is neglected and there is no other body force for the liquid plug.
- (3) The interface is flat and is vertical to the wall of the channel.
- (4) The microchannel has a high aspect ratio (height/width), hence the flow can be regarded as 2D.
- (5) The liquid plug does not slip on the wall of the channel.
- (6) The viscosity of the adjacent immiscible phase is negligible, and there is no shear stress on the free surface of the plug.
- (7) The liquid is an incompressible Newtonian fluid.

### 2.2. Governing equation and boundary conditions

For the Stokes flow in the plug, the governing equation is biharmonic

$$\nabla^4 \varphi = 0 \quad (1)$$

where  $\varphi$  is the stream function, which is defined as

$$u_r = \frac{1}{r} \frac{\partial \varphi}{\partial \theta} \quad (2)$$

$$u_\theta = -\frac{\partial \varphi}{\partial r} \quad (3)$$

This definition of  $\varphi$  satisfies the continuity equation automatically. This biharmonic equation is usually used to describe Stokes flow [37,38] and elastic mechanical problems [39]. In polar coordinate system, the biharmonic operator  $\nabla^4$  is

$$\nabla^4 = \left( \frac{\partial^2}{\partial r^2} + \frac{1}{r} \frac{\partial}{\partial r} + \frac{1}{r^2} \frac{\partial^2}{\partial \theta^2} \right) \left( \frac{\partial^2}{\partial r^2} + \frac{1}{r} \frac{\partial}{\partial r} + \frac{1}{r^2} \frac{\partial^2}{\partial \theta^2} \right) \quad (4)$$

The stream function is constant on the boundaries. Here, we set it to be zero.

$$\varphi(R_1, \theta) = \varphi(R_2, \theta) = \varphi(r, \theta_1) = \varphi(r, \theta_2) = 0 \quad (5)$$

The two ends of the plug are considered as free surfaces, because the viscosity of the air is negligible. The boundary conditions at these two ends are respectively

$$\begin{aligned} \frac{1}{r} \frac{\partial}{\partial \theta} u_\theta(r, \theta_1) &= \frac{1}{r^2} \frac{\partial^2}{\partial \theta^2} \varphi(r, \theta_1) = 0, \quad \frac{1}{r} \frac{\partial}{\partial \theta} u_\theta(r, \theta_2) \\ &= \frac{1}{r^2} \frac{\partial^2}{\partial \theta^2} \varphi(r, \theta_2) = 0 \end{aligned} \quad (6)$$

The speeds at the outer and the inner walls are  $V_{R1}$  and  $V_{R2}$  in the clockwise direction relative to the rotating frame of reference.

$$-\frac{\partial}{\partial r} \varphi(R_1, \theta) = -V_{R1} \quad (7)$$

$$-\frac{\partial}{\partial r} \varphi(R_2, \theta) = -V_{R2} \quad (8)$$

### 2.3. Nondimensionlization

Introducing the following dimensionless parameters,

$$\begin{aligned} \hat{r} &= \frac{r}{R_1}, \quad \hat{\theta} = \frac{\theta - \theta_1}{\theta_2 - \theta_1} = \frac{\theta - \theta_1}{\Delta\theta}, \quad \hat{u}_\theta = \frac{u_\theta}{V_{R1}}, \quad \hat{\varphi} = \frac{\varphi}{V_{R1}R_1}, \\ \hat{u}_r &= \frac{u_r(\theta_2 - \theta_1)}{V_{R1}} = u_r \frac{\Delta\theta}{V_{R1}} \end{aligned} \quad (9)$$

The dimensionless governing equation is

$$\left( \frac{\partial^2}{\partial \hat{r}^2} + \frac{1}{\hat{r}} \frac{\partial}{\partial \hat{r}} + \frac{1}{\hat{r}^2} \frac{\partial^2}{\partial \hat{\theta}^2} \right)^2 \hat{\varphi} = 0 \quad (10)$$

The radius ratio between the inner wall of the channel to the outer wall is defined as

$$\hat{R}_2 = R_2/R_1 \quad (11)$$

The dimensionless plug length is defined as

$$\hat{L} = L/(R_1 - R_2) \quad (12)$$

The dimensionless boundary conditions are

$$\hat{\varphi}(1, \hat{\theta}) = \hat{\varphi}(\hat{R}_2, \hat{\theta}) = 0 \quad (13)$$

$$\hat{\varphi}(\hat{r}, 0) = \hat{\varphi}(\hat{r}, 1) = 0 \quad (14)$$

$$\frac{\partial^2}{\partial \hat{\theta}^2} \hat{\varphi}(\hat{r}, 0) = \frac{\partial^2}{\partial \hat{\theta}^2} \hat{\varphi}(\hat{r}, 1) = 0 \quad (15)$$

$$\frac{\partial}{\partial \hat{r}} \hat{\varphi}(1, \hat{\theta}) = 1 \quad (16)$$

$$\frac{\partial}{\partial \hat{r}} \hat{\varphi}(\hat{R}_2, \hat{\theta}) = \hat{R}_2 \quad (17)$$

### 2.4. Analytical solution

The biharmonic equation Eq. (10) and its boundary conditions can be solved using FFT method. Its solution can be written as

$$\hat{\varphi}(\hat{r}, \hat{\theta}) = \sum_{n=0}^{\infty} [\phi_n(\hat{r}) \sin(n\pi\hat{\theta}) + \psi_n(\hat{r}) \cos(n\pi\hat{\theta})] \quad (18)$$

which is the Fourier expansion of  $\hat{\varphi}(\hat{r}, \hat{\theta})$ . According to the homogeneous boundary conditions Eqs. (14) and (15), we can write the solution in a simpler form

$$\hat{\varphi}(\hat{r}, \hat{\theta}) = \sum_{n=1}^{\infty} [\phi_n(\hat{r}) \sin(n\pi\hat{\theta})] \quad (19)$$

This format of solution Eq. (19) satisfies the boundary conditions Eqs. (14) and (15) automatically. Function  $\phi_n(\hat{r})$  can be solved according to the other four boundary conditions Eqs. (13), (16), and (17). Using FFT method, the stream function can be determined as

$$\begin{aligned} \hat{\varphi}(\hat{r}, \hat{\theta}) &= \sum_{n=1}^{\infty} \sin(n\pi\hat{\theta}) \left( \frac{C_{1n}}{\hat{r}^{\alpha_n}} + C_{2n} \hat{r}^{\alpha_n} + C_{3n} \hat{r}^{\alpha_n+2} + \frac{C_{4n}}{\hat{r}^{\alpha_n-2}} \right) \\ &+ \sum_{n=1}^{\infty} \sin(n\pi\hat{\theta}) \left[ \frac{C'_{1n}}{\hat{r}} + C'_{2n} \hat{r} + C'_{3n} \hat{r}^3 + C'_{4n} \hat{r} \ln(\hat{r}) \right] \end{aligned} \quad (20)$$

where  $\alpha_n = n\pi/\Delta\theta$ . The dimensionless velocity components in  $r$  direction and in  $\theta$  direction are respectively

$$\begin{aligned} \hat{u}_r(\hat{r}, \hat{\theta}) &= \sum_{n=1}^{\infty} n\pi \cos(n\pi\hat{\theta}) \left[ \frac{C_{1n}}{\hat{r}^{\alpha_n+1}} + C_{2n} \hat{r}^{\alpha_n-1} + C_{3n} \hat{r}^{\alpha_n+1} + \frac{C_{4n}}{\hat{r}^{\alpha_n-1}} \right] \\ &+ \sum_{n=1}^{\infty} n\pi \cos(n\pi\hat{\theta}) \left[ \frac{C'_{1n}}{\hat{r}^2} + C'_{2n} + C'_{3n} \hat{r}^2 + C'_{4n} \ln(\hat{r}) \right] \end{aligned} \quad (21)$$

$$\begin{aligned} \hat{u}_\theta(\hat{r}, \hat{\theta}) &= - \sum_{n=1}^{\infty} \sin(n\pi\hat{\theta}) \left[ \frac{-\alpha_n C_{1n}}{\hat{r}^{\alpha_n+1}} + \alpha_n C_{2n} \hat{r}^{\alpha_n-1} + C_{3n} (\alpha_n + 2) \hat{r}^{\alpha_n+1} \right. \\ &+ C_{4n} (2 - \alpha_n) \hat{r}^{1-\alpha_n} \left. \right] - \sum_{n=1}^{\infty} \sin(n\pi\hat{\theta}) \\ &\times \left[ -\frac{C'_{1n}}{\hat{r}^2} + C'_{2n} + 3C'_{3n} \hat{r}^2 + C'_{4n} (\ln(\hat{r}) + 1) \right] \end{aligned} \quad (22)$$

The constant coefficients in these equations can be obtained from the boundary conditions. For  $\alpha_n \neq 1$

$$D_n = \frac{1 - (-1)^n}{n\pi} \left[ \hat{R}_2^2 - \alpha_n^2 \hat{R}_2^{2\alpha_n} + (2\alpha_n^2 - 2) \hat{R}_2^{2+2\alpha_n} - \alpha_n^2 \hat{R}_2^{4+2\alpha_n} + \hat{R}_2^{2+4\alpha_n} \right] \quad (23)$$

$$\begin{aligned} C_{1n} &= D_n \left[ -\hat{R}_2^{4+\alpha_n} + (1 - \alpha_n) \hat{R}_2^{2+2\alpha_n} + \alpha_n \hat{R}_2^{4+2\alpha_n} + \alpha_n \hat{R}_2^{2+3\alpha_n} \right. \\ &+ (1 - \alpha_n) \hat{R}_2^{4+3\alpha_n} - \hat{R}_2^{2+4\alpha_n} \left. \right] \end{aligned} \quad (24)$$

$$\begin{aligned} C_{2n} &= D_n \left[ -\hat{R}_2^2 - \alpha_n \hat{R}_2^{2+\alpha_n} + (1 + \alpha_n) \hat{R}_2^{4+\alpha_n} + (1 + \alpha_n) \hat{R}_2^{2+2\alpha_n} \right. \\ &- \alpha_n \hat{R}_2^{4+2\alpha_n} - \hat{R}_2^{4+3\alpha_n} \left. \right] \end{aligned} \quad (25)$$

$$\begin{aligned} C_{3n} &= D_n \left[ \hat{R}_2^2 - \alpha_n \hat{R}_2^{2\alpha_n} + (-1 + \alpha_n) \hat{R}_2^{2+\alpha_n} - \alpha_n \hat{R}_2^{4+\alpha_n} + (-1 + \alpha_n) \hat{R}_2^{2+2\alpha_n} \right. \\ &+ \hat{R}_2^{2+3\alpha_n} \left. \right] \end{aligned} \quad (26)$$

$$\begin{aligned} C_{4n} &= D_n \left[ \alpha_n \hat{R}_2^{2\alpha_n} + \hat{R}_2^{2+\alpha_n} + (-1 - \alpha_n) \hat{R}_2^{2+2\alpha_n} + (-1 - \alpha_n) \hat{R}_2^{2+3\alpha_n} \right. \\ &+ \alpha_n \hat{R}_2^{4+3\alpha_n} + \hat{R}_2^{2+4\alpha_n} \left. \right] \end{aligned} \quad (27)$$

and for  $\alpha_n = 1$

$$D'_n = \frac{1 - (-1)^n}{2n\pi(1 + \hat{R}_2)[1 - \hat{R}_2^2 + \ln(\hat{R}_2) + \hat{R}_2^2 \ln(\hat{R}_2)]} \quad (28)$$

$$C'_{1n} = D'_n \hat{R}_2^2 [1 - \hat{R}_2^2 - 2\hat{R}_2 \ln(\hat{R}_2)] \quad (29)$$

$$C'_{2n} = D'_n [-1 + \hat{R}_2^4 + (-1 - \hat{R}_2 - \hat{R}_2^2 + \hat{R}_2^3) 2 \ln(\hat{R}_2)] \quad (30)$$

$$C'_{3n} = D'_n [1 - \hat{R}_2^2 + (1 + \hat{R}_2 + \hat{R}_2^2) 2 \ln(\hat{R}_2)] \quad (31)$$

$$C'_{4n} = D'_n [-2(-1 + \hat{R}_2)(1 + \hat{R}_2)^3] \quad (32)$$

The absolute dimensional velocity field of the liquid plug is

$$u'_\theta = V_{R1} \hat{u}_\theta + \omega r = V_{R1} \hat{u}_\theta + \frac{r}{R_1} V_{R1} \quad (33)$$

$$u'_r = \frac{V_{R1} \hat{u}_r}{\Delta\theta} \quad (34)$$

### 2.5. Resistance of the liquid plug

The moment of force balance diagram for the liquid plug is shown in Fig. 2. These forces are in moment balance for the low Reynolds number. The moment can be derived by integrating the shear stress along the wall of the channel. For unit depth of the channel, the moment of shear force that the inner wall applies to the liquid is

$$\begin{aligned} M_{f2} &= - \int_{\theta_1}^{\theta_2} \tau_{r\theta} r^2 d\theta \Big|_{r=R_2} \\ &= -\mu\Delta\theta R_1 V_{R1} \left[ \sum_{\substack{n=1 \\ \alpha_n \neq 1}}^{\infty} \frac{(-1)^n - 1}{n\pi} (\hat{R}_2) + \sum_{\alpha_n=1}^{\infty} \frac{(-1)^n - 1}{n\pi} Q(\hat{R}_2) \right] \end{aligned} \quad (35)$$

where

$$\begin{aligned} P(\hat{r}) &= \alpha_n(\alpha_n + 2) \hat{r}^{-\alpha_n} C_{1n} + \alpha_n(\alpha_n - 2) \hat{r}^{\alpha_n} C_{2n} + (\alpha_n \\ &\quad + 2) \alpha_n \hat{r}^{\alpha_n+2} C_{3n} + (\alpha_n - 2) \alpha_n \hat{r}^{-\alpha_n+2} C_{4n} \end{aligned} \quad (36)$$

$$Q(\hat{r}) = 3\hat{r}^{-1} C'_{1n} - \hat{r} C'_{2n} + 3\hat{r}^3 C'_{3n} - \hat{r} \ln(\hat{r}) C'_{4n} \quad (37)$$

The moment of shear force caused by the outer wall is

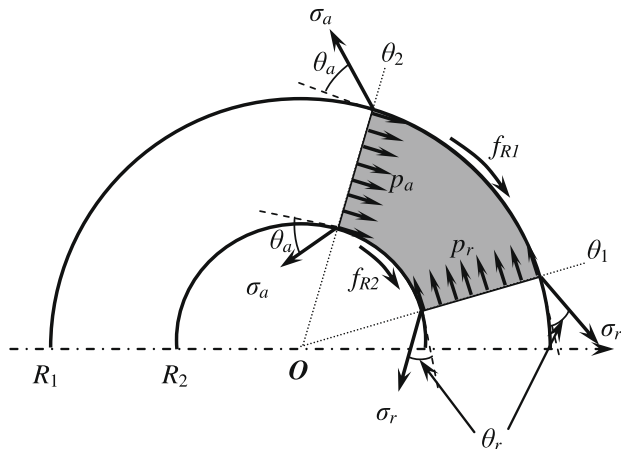


Fig. 2. Force balance diagram of the liquid plug.

$$M_{f1} = \mu\Delta\theta R_1 V_{R1} \left[ \sum_{\substack{n=1 \\ \alpha_n \neq 1}}^{\infty} \frac{(-1)^n - 1}{n\pi} P(1) + \sum_{\alpha_n=1}^{\infty} \frac{(-1)^n - 1}{n\pi} Q(1) \right] \quad (38)$$

Although we assume flat interfaces (assumption 3 in Section 2.1) in the 2D model, the effect of surface tension and contact angle hysteresis on the dynamics of the plug can be included in the moment of force balance. The surface tension and the contact angle influence the plug speed, while the plug speed influences the flow field in the plug. In this way, the effect of the surface tension and contact angle on the flow field of the plug can be considered indirectly through the plug speed. The moments of surface tension force at the advancing and receding ends are respectively

$$M_{adv} = \sigma_{adv} (R_1 + R_2) \cos(\theta_{adv}) \quad (39)$$

$$M_{rec} = \sigma_{rec} (R_1 + R_2) \cos(\theta_{rec}) \quad (40)$$

where  $\theta_{adv}$  and  $\theta_{rec}$  are the advancing and receding contact angles, and  $\sigma_{adv}$  and  $\sigma_{rec}$  denote the surface tension at the advancing and receding ends, respectively. The moment balance equation is

$$\int_{R_i}^{R_o} \Delta p r dr = M_{f1} + M_{f2} + M_{rec} - M_{adv} \quad (41)$$

where  $\Delta p = p_{rec} - p_{adv}$  is the pressure drop from the receding end to the advancing end of the plug. This leads to the driving pressure

$$\begin{aligned} \Delta p &= \frac{2\mu\Delta\theta R_1 V_{R1}}{(R_1^2 - R_2^2)} \left\{ \sum_{\substack{n=1 \\ \alpha_n \neq 1}}^{\infty} \frac{(-1)^n - 1}{n\pi} [P(1) - P(\hat{R}_2)] + \sum_{\substack{n=1 \\ \alpha_n=1}}^{\infty} \frac{(-1)^n - 1}{n\pi} \right. \\ &\quad \times [Q(1) - Q(\hat{R}_2)] \left. \right\} + \frac{2[\sigma_{rec} \cos(\theta_{rec}) - \sigma_{adv} \cos(\theta_{adv})]}{R_1 - R_2} \end{aligned} \quad (42)$$

In Eq. (42), the first term is caused by the friction, and the second term is caused by the surface tension and contact angles.

To actuate the plug, we can use pressure to overcome the friction and the surface tension. But for different channel geometries, plug speeds and fluid properties, the driving pressure cannot be compared directly. Here, we used a dimensionless parameter, the plug resistance coefficient  $C_f$ , to characterize the flow resistance caused by a single plug. The plug resistance coefficient  $C_f$  is the product of the Moody friction factor  $f$  and the Reynolds number  $Re$ . The characteristic velocity is the average speed of the plug along the centre line of the channel  $V_{avg} = \omega(R_1 + R_2)/2$ , and the characteristic length is the width of the channel,  $(R_1 - R_2)$ . Therefore, the Reynolds number and the Moody friction factor are respectively

$$f = \frac{4\Delta p (R_1 - R_2)}{\Delta\theta (R_1 + R_2) \rho V_{avg}^2} \quad (43)$$

$$Re = \frac{\rho V_{avg} (R_1 - R_2)}{\mu} \quad (44)$$

Hence the plug resistance coefficient is given by

$$\begin{aligned} C_f = fRe &= \frac{8R_1(R_1 - R_2)}{(R_1 + R_2)^2} \left\{ \sum_{\substack{n=1 \\ \alpha_n \neq 1}}^{\infty} \frac{(-1)^n - 1}{n\pi} [P(1) - P(\hat{R}_2)] \right. \\ &\quad + \sum_{\substack{n=1 \\ \alpha_n=1}}^{\infty} \frac{(-1)^n - 1}{n\pi} [Q(1) - Q(\hat{R}_2)] \left. \right\} \\ &\quad + \frac{8(R_1 - R_2)[\sigma_{rec} \cos(\theta_{rec}) - \sigma_{adv} \cos(\theta_{adv})]}{\mu\Delta\theta (R_1 + R_2) V_{avg}} \end{aligned} \quad (45)$$

## 2.6. Validation by 1D model

Assuming that the liquid plug is infinitely long ( $\hat{L} \rightarrow \infty$ ), we can neglect the velocity component in the  $r$  and  $z$  directions.

$$u_r = u_z = 0 \quad (46)$$

Then the momentum equation for the Stokes flow in the curved channel is

$$\frac{d^2 u_{\theta,1D}}{dr^2} + \frac{1}{r} \frac{du_{\theta,1D}}{dr} - \frac{1}{r^2} u_{\theta,1D} = \frac{1}{\mu r} \frac{dp}{d\theta} \quad (47)$$

The boundary condition is

$$u_{\theta,1D}(R_1) = u_{\theta,1D}(R_2) = 0 \quad (48)$$

The solution of this 1D model is

$$u_{\theta,1D}(r) = \frac{1}{2\mu} \frac{dp}{d\theta} \times \left[ -\frac{R_1^2 \ln R_1 - R_2^2 \ln R_2}{R_1^2 - R_2^2} r + \frac{(\ln R_1 - \ln R_2) R_1^2 R_2^2}{R_1^2 - R_2^2} \frac{1}{r} + r \ln r \right] \quad (49)$$

The average velocity is

$$V_{\text{avg},1D} = \frac{1}{R_1 - R_2} \int_{R_2}^{R_1} u_{\theta,1D}(r) dr = -\frac{1}{2\mu} \frac{dp}{d\theta} \times \frac{(R_1^2 - R_2^2 + 2R_1 R_2 (\ln R_1 - \ln R_2)) [R_1^2 - R_2^2 - 2R_1 R_2 (\ln R_1 - \ln R_2)]}{4(R_1 - R_2)^2 (R_1 + R_2)} \quad (50)$$

According to Eq. (33), the dimensionless relative velocity can be obtained after some rearrangement,

$$\hat{u}_{\theta,1D} = \frac{u_{\theta,1D}}{V_{R1}} - \frac{r}{R_1} = \frac{u_{\theta,1D}}{V_{\text{avg},1D}} \frac{(R_1 + R_2)}{2R_1} - \frac{r}{R_1} = -\hat{r} + \frac{2(1 - \hat{R}_2^2)}{(1 - \hat{R}_2^2)^2 - 4\hat{R}_2^2 \ln^2(\hat{R}_2)} \times \left[ \hat{R}_2^2 \ln(\hat{R}_2) \frac{1}{\hat{r}} + (\hat{R}_2^2 - 1) \hat{r} \ln(\hat{r}) - \hat{R}_2^2 \ln \hat{R}_2 \hat{r} \right] \quad (51)$$

where the dimensionless variables  $\hat{r}$  and  $\hat{R}_2$  are used.

If the length of the liquid plug tends to infinity ( $\hat{L} \rightarrow \infty$ ), the flow can be simplified to 1D. For the dimensionless plug lengths  $\hat{L} = 100$ , the 2D solution for different radius ratios at cross section **X–X** of the plug reduces to the 1D solution, as shown in Fig. 3. The radial position is defined as  $x = (\hat{r} - \hat{R}_2)/(1 - \hat{R}_2)$ . The velocity pro-

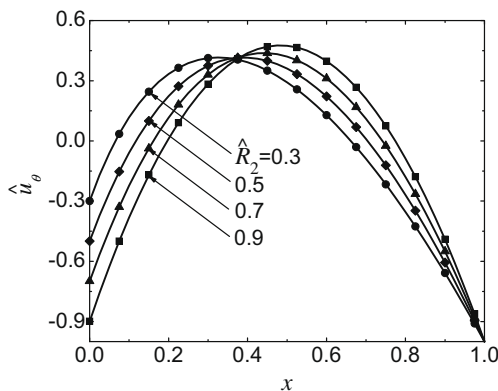


Fig. 3. Validation of the 2D model by the 1D solution (lines: 1D solution; symbols: 2D solution).

file along this cross section is much like the Couette flow with pressure gradient.

## 3. Results and discussion

### 3.1. Comparison between 2D model and experiment

According to Eqs. (20–22), the streamlines and the velocity field in a typical plug is depicted in Fig. 4, which give a clear picture of the overall flow pattern. The streamlines in Fig. 4a shows the two vortices near the inner and outer walls. Fig. 4b presents the dimensionless velocity field. The inner wall vortex **A** is in anticlockwise direction (positive  $\hat{\phi}_A$ ), while the outer wall vortex **B** (negative  $\hat{\phi}_B$ ) is in clockwise direction. To draw the contour lines of dimensionless stream function  $\hat{\phi}$ , we use the increments of  $\Delta\hat{\phi} = 0.002$ . As shown in Fig. 4a, vortex **B** is larger than vortex **A**, due to the curvature effect. One streamline **S–S** separates these two vortices such that  $\hat{\phi}_{S-S} = 0$  and no particle can cross this streamline by advection. Fig. 4c is the measured  $\mu$ PIV velocity field by Fries et al. [14]. The dimensionless plug length  $\hat{L} = 1.6$  in Fig. 4c is calculated in pixel from the image by a Matlab program, where

$$\hat{L} = \frac{\text{area of plug in pixel}}{(\text{width of plug in pixel})^2} \quad (52)$$

The two counter rotating vortices in Fig. 4c can be clearly observed. The comparison with the experimental results shows that the 2D analytical model for microchannel with high aspect ratio captures the large part of the essential of the flow field, even though the  $\mu$ PIV measurement was carried out in a three-dimensional microchannel with an aspect ratio of 1.

The influence of curvature in a discrete flow is different from the single-phase flow. Continuous single-phase flow travelling through curved channels experiences interplay between inertial forces acting to direct axial motion and centrifugal effects acting along the conduit's radius of curvature. Under appropriate conditions, these effects establish a radial pressure gradient whose magnitude can become sufficient to generate the transverse Dean vortices [40]. These transverse Dean vortices expand interfacial area between species through stretching and folding and can enhance mixing [30,31,41]. The flow resistance in the curved channel is larger than that in the straight channel [42]. Heat transfer between the fluid and the twisted pipe can be more effective [43,44]. As plugs move through a straight microchannel, recirculating flow is generated due to the presence of the interfaces [33]. The two vortices in the liquid plug are of equal size due to the symmetrical effect of the channel walls. As the droplet/plug travels through a curved channel, the two halves of the plug experience unequal recirculating flows. One half of the plug is exposed to the inner arc of the curved channel, a shorter channel path, and thus a small recirculating flow is generated compared to the other half of the plug which is exposed to the outer arc with a longer channel path. Hence, the two vortices become asymmetrical.

### 3.2. Velocity profiles

#### 3.2.1. Effect of curvature

In order to analyze the effect of the channel curvature on the flow profile along the cross section **X–X**, we fixed the dimensionless plug length at  $\hat{L} = 1$  and vary the curvature of the channel by changing  $\hat{R}_2$ . Fig. 5a shows the velocity profile  $\hat{u}_\theta$  along **X–X** for different curvatures. The maximum velocity increases with the increase of  $\hat{R}_2$ . The velocity component  $\hat{u}_\theta$  is nearly symmetric for  $\hat{R}_2 = 0.9$  due to the low curvature of the microchannel, as shown in Fig. 5a.



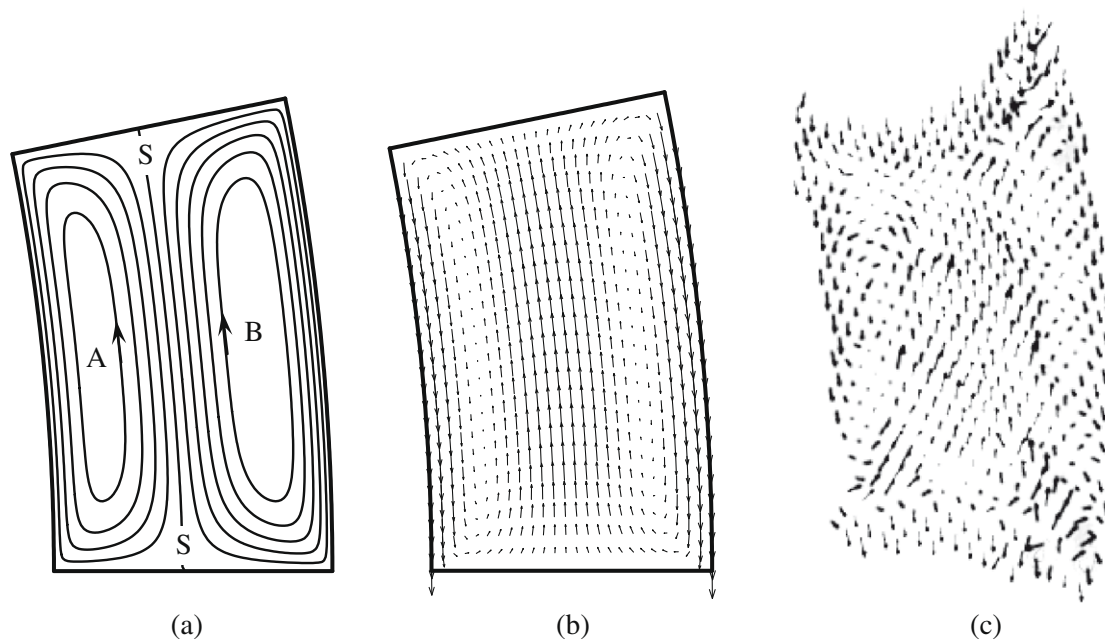


**Fig. 4.** Velocity field in a plug with dimensionless plug length  $\hat{L} = 1.6$  and radius ratio  $\hat{R}_2 = 0.8824$ , (a) streamlines with incremental of dimensionless stream function  $\Delta\hat{\phi} = 0.002$ , (b) dimensionless velocity field, and (c) velocity field obtained by  $\mu$ PIV (reprinted with permission from Ref. [14]).

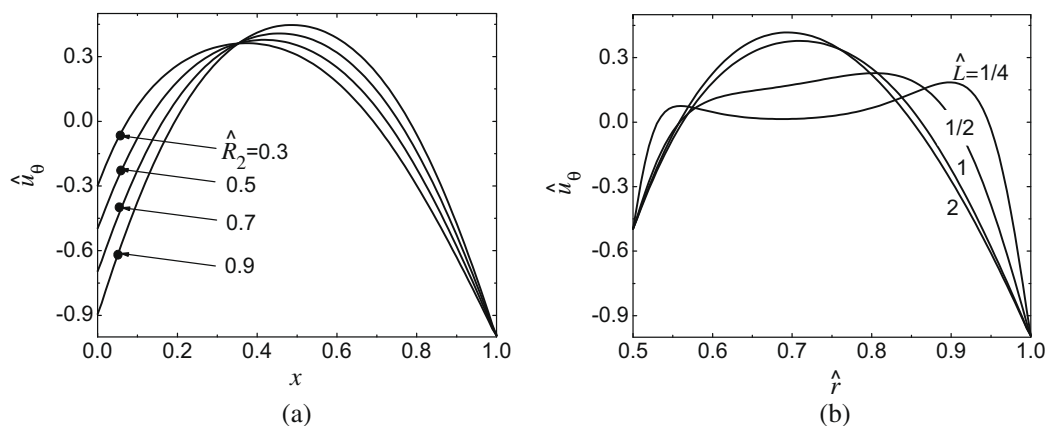


**Fig. 5.** Dimensionless velocity component  $\hat{u}_\theta$  at the cross section **X–X**, (a) for different radius ratios  $\hat{R}_2$  (dimensionless plug length is fixed at  $\hat{L} = 1$ ), (b) for different dimensionless plug lengths  $\hat{L}$  (radius ratio is fixed at  $\hat{R}_2 = 0.5$ ).

### 3.2.2. Effect of dimensionless plug length

To analyze the effect of the dimensionless plug length on the velocity profile, the radius ratio is kept at  $\hat{R}_2 = 0.5$ . Fig. 5b presents  $\hat{u}_\theta$  along cross section **X–X** for different dimensionless plug lengths. The results clearly show that the dimensionless plug length influences the flow field. For long plugs ( $\hat{L} = 2$  in Fig. 5b), the velocity profile is consistent with results reported in Fig. 3. For short plugs ( $\hat{L} = 1/4$  in Fig. 5b), there are two local maximum points of velocity, as vortices **A** and **B** move towards the inner wall and outer wall respectively, which will be explained in the following subsection.

### 3.3. Vortex centres

From the physical meaning of the stream function, the change in stream function between two points is equal to the volume flow rate of fluid passing through a line between the two points. As the stream function at the boundary is 0, the extreme points of the stream function in the plug correspond to the vortex centres, and the magnitude of the stream function reflects the strength of the

vortex. Hence the location of the vortex centre and the value of the stream function at the vortex centre are important parameters to quantify the vortex pattern in the plug. As the stream function is symmetric with respect to the cross section **X–X**, the vortex centres are located along **X–X**. To quantify the effects of the plug lengths and the curvature, the radial position of the vortex centre in the  $r$  direction ( $x_A$  and  $x_B$ ) versus  $\hat{L}$  and  $\hat{R}_2$  are shown in Fig. 6a and b, while the corresponding dimensionless stream functions at the vortex centres ( $\hat{\phi}_{A,\max}$  and  $\hat{\phi}_{B,\min}$ ) are shown in Fig. 6c and d, respectively.

#### 3.3.1. Effect of curvature

The movement of the vortex centre location ( $x_A$  and  $x_B$ ) versus channel curvature (Fig. 6a and b) shows that for a given plug length, the vortex centres  $x_A$  and  $x_B$  move towards the direction of the inner wall as the channel curvature is increased (that is  $\hat{R}_2$  is decreased). When the channel curvature is increased,  $\hat{\phi}_{B,\min}$  increases (Fig. 6d), and the outer vortex **B** increases in size and strength and compress the inner vortex **A**. Fig. 6c shows that the

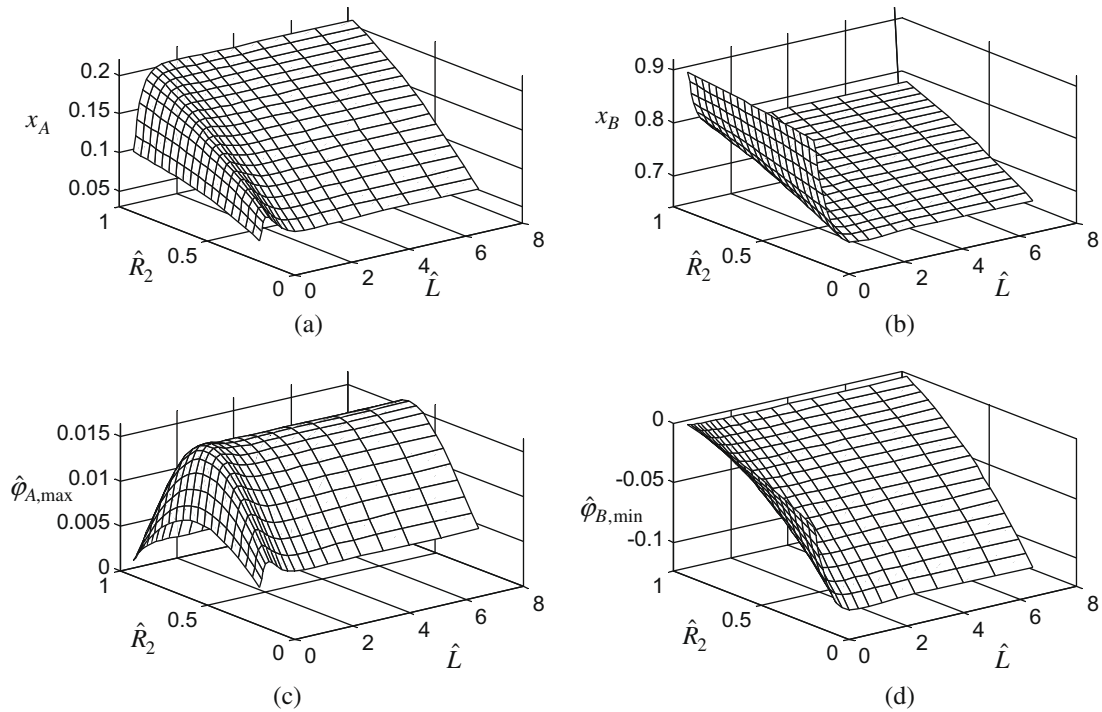


**Fig. 6.** Vortex centres and stream functions versus the dimensionless plug length and the radius ratio. (a) location of vortex centre of vortex **A**, (b) location of vortex centre of vortex **B**, (c) stream function at the vortex centre of vortex **A**, and (d) stream function at the vortex centre of vortex **B**.

magnitude of the dimensionless stream function  $\hat{\phi}_{A,\max}$  is small and the inner vortex **A** is relatively weak. This effect of increasing curvature on the flow patterns can also be clearly observed in Fig. 7. Fig. 7a–f illustrate the effect of channel curvature at different fixed dimensionless plug lengths  $\hat{L} = 1/4, 1/2$  and 1 respectively.

### 3.3.2. Effect of dimensionless plug length

Fig. 6a and b show that the movement of the vortex centre and the corresponding dimensionless stream functions with channel curvatures and dimensionless plug lengths.

It is demonstrated that for a relative low channel curvature (large  $\hat{R}_2$ ), the flow patterns depend on the dimensionless plug length as shown in Fig. 7a, c and e. Since channel curvature effect is small, the vortices are nearly symmetrical about the streamline **S–S**. Initially, with the increase of plug length, both vortices **A** and **B** increase in size and strength. The vortex centres  $x_A$  and  $x_B$  move rapidly towards the streamline **S–S**, the magnitude of  $\hat{\phi}_{A,\max}$  and  $\hat{\phi}_{B,\min}$  both increase as vortices **A** and **B** expand. For relatively large dimensionless plug length ( $\hat{L} > \hat{L}_{\text{long}}$ ) the vortex centres  $x_A$  and  $x_B$  becomes almost fixed in their locations. Here  $\hat{L}_{\text{long}}$  refers to the dimensionless plug length where  $\hat{u}_\theta$  along **X–X** approaches the fully developed velocity profile as shown in Fig. 3. The unchanged velocity profiles make the locations of the vortex centres nearly constant.

For a relative high channel curvature (small  $\hat{R}_2$ ), the movement of the vortex centres strongly depends on the dimensionless plug length  $\hat{L}$ , as shown in Fig. 7b, d and f. Initially, with the increase of  $\hat{L}$ , vortices **A** and **B** increase in size and strength, just like the plugs with low curvatures. The vortex centres  $x_A$  and  $x_B$  move rapidly towards the streamline **S–S**, and the magnitudes of  $\hat{\phi}_{A,\max}$  and  $\hat{\phi}_{B,\min}$  increase as vortices **A** and **B** expand. However, due to the channel curvature, vortex **B** expands faster than vortex **A**. If the plug length increase to a value beyond  $\hat{L}_m$ , the vortices will develop to such an extent that the inner vortex **A** is compressed by the outer vortex **B**. Vortex centres  $x_A$  moves towards the direction of the inner wall while  $x_B$  move towards the streamline **S–S** as vortex **B**

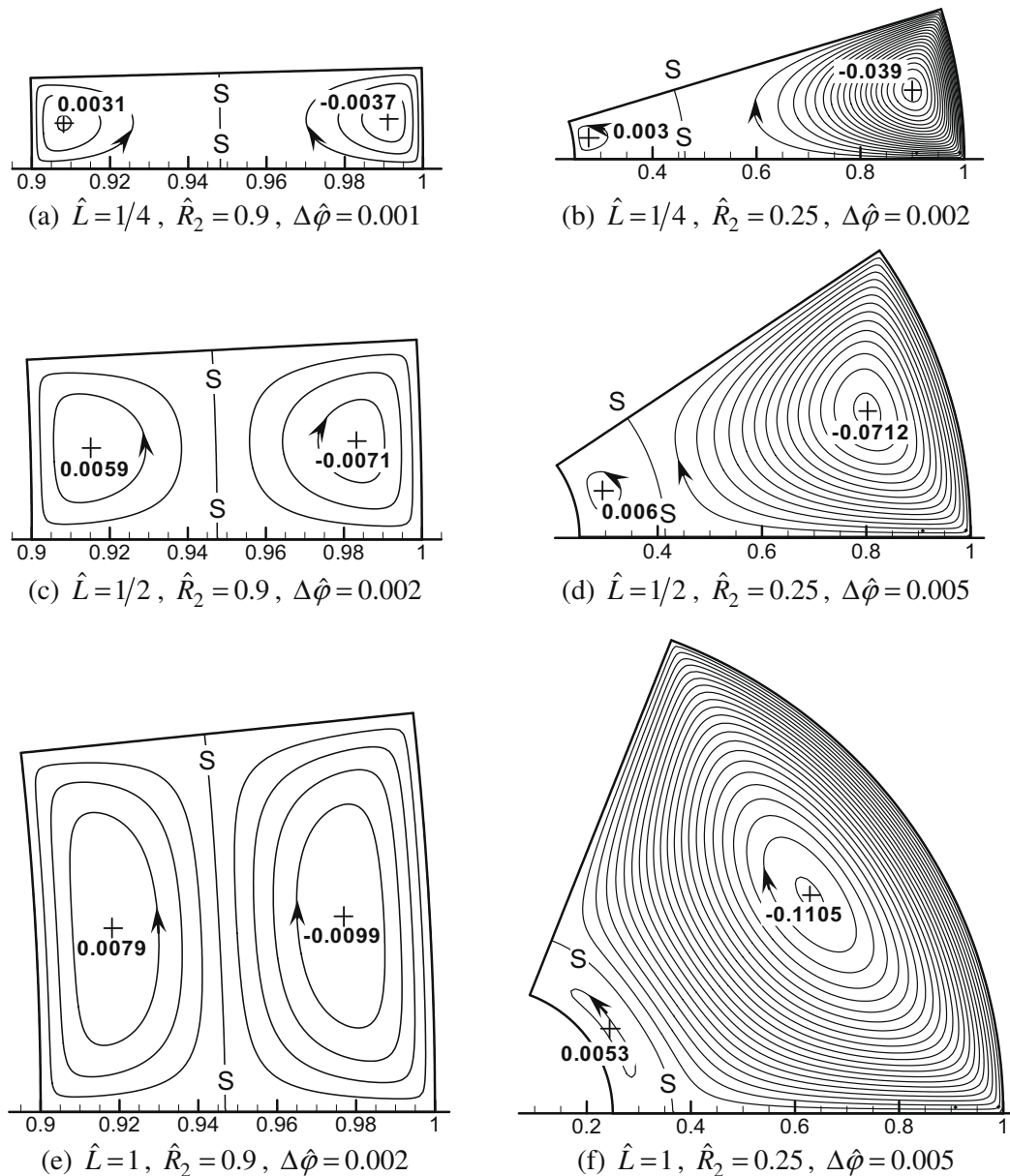
expands. For example,  $\hat{L}_m$  is 0.54 when  $\hat{R}_2$  is fixed at 0.25. Similarly to the case of low channel curvatures, at relatively large dimensionless plug lengths ( $\hat{L} > \hat{L}_{\text{long}}$ ), the vortex centres  $x_A$  and  $x_B$  becomes almost fixed in their locations.

### 3.4. The plug resistance coefficient

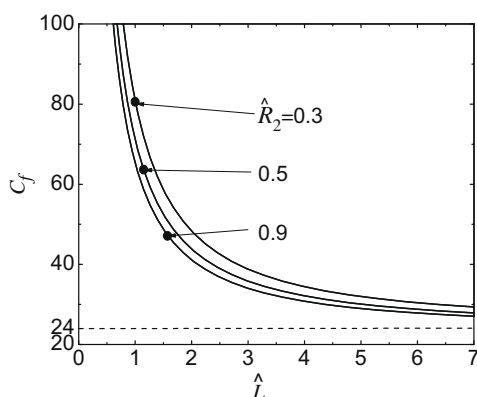
According to Eq. (40), the plug resistance coefficient  $C_f$  is influenced by the shear force and the surface tension. For the surface tension contribution (the second term on the right hand side of Eq. (45)), although there are many factors influencing the plug flow resistance  $C_f$ , the relationships between plug resistance coefficient  $C_f$  and the parameters, such as viscosity  $\mu$ , plug speed  $V_{\text{avg}}$ , contact angles  $\theta_{\text{adv}}$  and  $\theta_{\text{rec}}$ , surface tension  $\sigma$ , are straightforward. In addition, the surface tension contribution to plug resistance coefficient is small or even negligible for the cases of small variation of surface tension ( $\sigma_{\text{rec}} - \sigma_{\text{adv}}$ ) and small contact angle hysteresis [ $\cos(\theta_{\text{rec}}) - \cos(\theta_{\text{adv}})$ ] [45]. Hence, only the contribution of shear force to the plug resistant coefficient (the first term on the right hand side of Eq. (45)) is considered in the following analysis.

Fig. 8 shows the plug resistance coefficient variation with the increase of the dimensionless plug length for different radius ratios. As the dimensionless plug length increases, plug resistance coefficient decreases dramatically, and approaches an asymptotic limit. This can be explained by the high velocity gradient at the end of the plug, which causes large flow resistance. Hence short plugs experience large resistance coefficient. It is also shown that for small radius ratio  $\hat{R}_2$ , the curvature causes high resistance of the plug flow.

For continuous laminar flow between two parallel plates, in the fully developed region, the resistance coefficient can be obtained using its parabolic velocity profile. The resistance coefficient is 24 by using the average velocity as the characteristic velocity [46]. The plug resistance coefficients are always larger than 24. And this value is the asymptotic limit when  $\hat{L} \rightarrow \infty$  and  $\hat{R}_2 \rightarrow 1$ , as shown in Fig. 8. For example, for  $\hat{R}_2 = 0.9$  and  $C_f = 24.24$  (that



**Fig. 7.** Streamlines in plugs with different dimensionless plug lengths and different curvatures. The crosses and the corresponding values indicate the locations and stream functions of the vortex centres, respectively. The arrows indicate the direction of recirculation.



**Fig. 8.** Plug resistance coefficient  $C_f$  decreases with the dimensionless plug length  $\hat{L}$  for different radius ratios  $\hat{R}_2$ .

is 1% deviation from 24), the corresponding dimensionless plug length is  $\hat{L} = 84.4$ . Under this condition, the plug behaves as if it is fully developed continuous flow between parallel plates. Therefore, when  $\hat{R}_2 = 0.9$  and  $\hat{L} < 84.4$ , the idealization of a long plug in a curved channel as fully developed continuous flow between parallel plates cannot provide an accurate prediction of the pressure loss.

#### 4. Conclusions

This paper analytically investigates plug flow in curved microchannels. We use the Finite Fourier Transform method to solve the biharmonic equation and get the series solution of the stream functions. The plug resistance coefficient is derived from the moment balance of the plug. The results show that for the plug moving in microchannel with low curvature, the vortex centres shift towards the wall of the microchannel when the dimensionless plug



length is decreased. For a given plug length, the vortex centres move towards the direction of the inner wall as the channel curvature is increased. The plug flow resistance was analyzed and the result showed that the plug flow resistance coefficient decreases with the increase of the dimensionless plug length and with the decrease of the microchannel curvature. The flow resistance coefficient tends to the asymptotic value of 24 as the dimensionless plug length tends to infinity and the radius ratio approaches to one.

## Acknowledgements

The authors would like to thank the Agency of Science, Technology and Research, Singapore A\*Star, SERC Grant No. 0521010108, “Droplet-based micro/nanofluidics” for its financial support.

## References

- [1] S.-Y. Teh, R. Lin, L.-H. Hung, A.P. Lee, Droplet microfluidics, *Lab Chip* 8 (2) (2008) 198–220.
- [2] M. Prakash, N. Gershenfeld, Microfluidic bubble logic, *Science* 315 (5813) (2007) 832–835.
- [3] L.F. Cheow, L. Yobas, D.L. Kwong, Digital microfluidics: droplet based logic gates, *Appl. Phys. Lett.* 90 (5) (2007) 054107.
- [4] B.J. Adzima, S.S. Velankar, Pressure drops for droplet flows in microfluidic channels, *J. Micromechan. Microeng.* 16 (8) (2006) 1504–1510.
- [5] T.S. Sammarco, M.A. Burns, Thermocapillary pumping of discrete drops in microfabricated analysis devices, *AIChE J.* 45 (2) (1999) 350–366.
- [6] N.T. Nguyen, X. Huang, Thermocapillary effect of a liquid plug in transient temperature fields, *Jpn. J. Appl. Phys.* 1 44 (2) (2005) 1139–1142.
- [7] N.T. Nguyen, W.W. Pang, X. Huang, Sample transport with thermocapillary force for microfluidics, *J. Phys.: Confer. Ser.* 34 (1) (2006) 967–972.
- [8] M.G. Pollack, R.B. Fair, A.D. Shenderov, Electrowetting-based actuation of liquid droplets for microfluidic applications, *Appl. Phys. Lett.* 77 (11) (2000) 1725–1726.
- [9] F. Mugele, J.C. Baret, Electrowetting: from basics to applications, *J. Phys.: Cond. Matter* 17 (28) (2005) R705–R774.
- [10] N.T. Nguyen, K.M. Ng, X. Huang, Manipulation of ferrofluid droplets using planar coils, *Appl. Phys. Lett.* 89 (5) (2006) 52509.
- [11] R. Wang, K. Hashimoto, A. Fujishima, M. Chikuni, E. Kojima, A. Kitamura, M. Shimohigoshi, T. Watanabe, Light-induced amphiphilic surfaces, *Nature* 388 (6641) (1997) 431–432.
- [12] A. Wixforth, Acoustically driven planar microfluidics, *Superlatt. Microstruct.* 33 (5–6) (2003) 389–396.
- [13] Z.J. Jiao, X.Y. Huang, N.T. Nguyen, Scattering and attenuation of surface acoustic waves in droplet actuation, *J. Phys. A: Math. Theor.* 41 (35) (2008) 355502.
- [14] D.M. Fries, S. Waelchli, P. Rudolf von Rohr, Gas–liquid two-phase flow in meandering microchannels, *Chem. Eng. J.* 135 (Suppl. 1) (2008) S37–S45.
- [15] C. Wang, N.T. Nguyen, T.N. Wong, Optical measurement of flow field and concentration field inside a moving nanoliter droplet, *Sensors Actuators A: Phys.* 133 (2 SPEC. ISS.) (2007) 317–322.
- [16] M.N. Kashid, I. Gerlach, S. Goetz, J. Franzke, J.F. Acker, F. Platte, D.W. Agar, S. Turek, Internal circulation within the liquid slugs of a liquid–liquid slug-flow capillary microreactor, *Indus. Eng. Chem. Res.* 44 (14) (2005) 5003–5010.
- [17] C. King, E. Walsh, R. Grimes, PIV measurements of flow within plugs in a microchannel, *Microfluid. Nanofluid.* 3 (4) (2007) 463–472.
- [18] H. Kinoshita, S. Kaneda, T. Fujii, M. Oshima, Three-dimensional measurement and visualization of internal flow of a moving droplet using confocal micro-PIV, *Lab Chip* 7 (3) (2007) 338–346.
- [19] D.M. Fries, P.R. von Rohr, Liquid mixing in gas–liquid two-phase flow by meandering microchannels, *Chem. Eng. Sci.* 64 (6) (2009) 1326–1335.
- [20] J.D. Tice, H. Song, A.D. Lyon, R.F. Ismagilov, Formation of droplets and mixing in multiphase microfluidics at low values of the Reynolds and the capillary numbers, *Langmuir* 19 (22) (2003) 9127–9133.
- [21] A. Günther, S.A. Khan, M. Thalmann, F. Trachsel, K.F. Jensen, Transport and reaction in microscale segmented gas–liquid flow, *Lab Chip* 4 (4) (2004) 278–286.
- [22] N. Harries, J.R. Burns, D.A. Barrow, C. Ramshaw, A numerical model for segmented flow in a microreactor, *Int. J. Heat Mass Transfer* 46 (17) (2003) 3313–3322.
- [23] W. Tanthapanichakoon, N. Aoki, K. Matsuyama, K. Mae, Design of mixing in microfluidic liquid slugs based on a new dimensionless number for precise reaction and mixing operations, *Chem. Eng. Sci.* 61 (13) (2006) 4220–4232.
- [24] M.N. Kashid, D.W. Agar, S. Turek, CFD modelling of mass transfer with and without chemical reaction in the liquid–liquid slug flow microreactor, *Chem. Eng. Sci.* 62 (18–20) (2007) 5102–5109.
- [25] M. Muradoglu, A. Günther, H.A. Stone, A computational study of axial dispersion in segmented gas–liquid flow, *Phys. Fluids* 19 (7) (2007) 072109.
- [26] R. Scardovelli, S. Zaleski, Direct numerical simulation of free-surface and interfacial flow, *Ann. Rev. Fluid Mech.* 31 (1999) 567–603.
- [27] T. Taha, Z.F. Cui, Hydrodynamics of slug flow inside capillaries, *Chem. Eng. Sci.* 59 (6) (2004) 1181–1190.
- [28] S. Osher, R.P. Fedkiw, Level set methods: an overview and some recent results, *J. Computat. Phys.* 169 (2) (2001) 463–502.
- [29] H. Fujioka, J.B. Grotberg, Steady propagation of a liquid plug in a two-dimensional channel, *J. Biomechan. Eng.* 126 (5) (2004) 567–577.
- [30] J.M. Ottino, *The Kinematics of Mixing: Stretching, Chaos, and Transport*, Cambridge University Press, New York, 1989.
- [31] H. Aref, The development of chaotic advection, *Phys. Fluids* 14 (4) (2002) 1315–1325.
- [32] H. Song, J.D. Tice, R.F. Ismagilov, A microfluidic system for controlling reaction networks in time, *Angewandte Chemie – International Edition* 42 (7) (2003) 768–772.
- [33] K. Handique, M.A. Burns, Mathematical modeling of drop mixing in a slit-type microchannel, *J. Micromechan. Microeng.* 11 (5) (2001) 548–554.
- [34] D. Kroujiline, H.A. Stone, Chaotic streamlines in steady bounded three-dimensional Stokes flows, *Phys. D: Nonlinear Phenom.* 130 (1–2) (1999) 105–132.
- [35] Z.B. Stone, H.A. Stone, Imaging and quantifying mixing in a model droplet micromixer, *Phys. Fluids* 17 (6) (2005) 1–11.
- [36] W.M. Deen, *Analysis of Transport Phenomena*, Oxford University Press, New York, 1998.
- [37] V.V. Meleshko, Steady stokes flow in a rectangular cavity, *Proc. R. Soc. Lond. Ser. A* 452 (1952) (1996) 1999–2022.
- [38] P.N. Shankar, *Slow Viscous Flows: Qualitative Features and Quantitative Analysis Using Complex Eigenfunction Expansions*, Imperial College Press, London, 2007.
- [39] S. Timoshenko, *Theory of Elasticity*, second ed., McGraw-Hill, New York, 1951.
- [40] W.R. Dean, Fluid motion in a curved channel, *Proc. R. Soc. Lond. Ser. A* 121 (787) (1928) 402–420.
- [41] S.W. Jones, O.M. Thomas, H. Aref, Chaotic advection by laminar flow in a twisted pipe, *J. Fluid Mech.* 209 (1989) 335–357.
- [42] W.H. Yang, J.Z. Zhang, H.E. Cheng, The study of flow characteristics of curved microchannel, *Appl. Therm. Eng.* 25 (13) (2005) 1894–1907.
- [43] A. Nakayama, N. Kokubo, T. Ishida, F. Kuwahara, Conjugate numerical model for cooling a fluid flowing through a spiral coil immersed in a chilled water container, *Numer. Heat Transfer; A: Appl.* 37 (2) (2000) 155–165.
- [44] L. Wang, F. Liu, Forced convection in slightly curved microchannels, *Int. J. Heat Mass Transfer* 50 (5–6) (2007) 881–896.
- [45] P.G. de Gennes, Wetting: statics and dynamics, *Rev. Mod. Phys.* 57 (3) (1985) 827–863.
- [46] F.M. White, *Fluid Mechanics*, Fifth ed., McGraw-Hill, Boston, 2002.